Ann. Geophys., 44, 287–301, 2026
https://doi.org/10.5194/angeo-44-287-2026

Annales Geophysicae
Open Access
EGU

Effect of a non-hydrostatic core-mantle boundary on the nutations and Length-of-day of Mars

Marta Folgueira López[1], **Véronique Dehant**[2,3], **Mihaela Puica**[4], **and Tim Van Hoolst**[2]

[1]Department Physics of the Earth and Astrophysics, Faculty of Mathematical Sciences, Plaza de Ciencias 3. Universidad Complutense de Madrid, Madrid, 28040, Spain
[2]Service Reference frames and planetology, Royal Observatory of Belgium, Brussels, 1180, Belgium
[3]Earth and Life Institute (ELI), Université catholique de Louvain (UCLouvain), Louvain-la-Neuve, 1348, Belgium
[4]Department of Mathematics, University of Oslo, Oslo, 0316, Norway

Correspondence: Marta Folgueira López (martafl@mat.ucm.es)

Received: 10 November 2025 – Discussion started: 22 December 2025
Revised: 20 March 2026 – Accepted: 24 March 2026 – Published: 23 April 2026

Abstract. Dynamic loads in planetary mantles have the potential to deform the core-mantle boundary (CMB). On Earth, subducting slabs primarily induce a degree 2–order 2 deformation of the CMB in the spherical harmonic (SH) reference system. On Mars, the presence of the dichotomy and of the Tharsis region could produce loading across multiple degrees and orders, including degree-1, degree 2–order 2, degree 2–order 0, and degree 3–order 3 components. Thanks to the InSight (Interior exploration using Seismic Investigations, Geodesy, and Heat Transport) mission's radio science experiment, observations of Mars' nutations are now available. Periodic length-of-day (LOD) variations of Mars have been detected first by radio tracking the Viking landers, and InSight data have indicated the presence of a secular trend in LOD. In the case of nutations, the Martian core's non-hydrostatic flattening plays a first-order role in determining nutation amplitudes. In this study, we explore second-order effects arising from dynamic topography at the CMB. We compute the pressure exerted on the CMB topography inside Mars' liquid core and evaluate the resulting topographic pressure torque acting on the boundary, which can influence both nutations and LOD variations. Our results show that, albeit at microarcsecond (μarcsec) level – well below current observational thresholds, the most significant contribution to nutations arises from degree 2–order 2 component. As for LOD variations, while Earth exhibits notable contributions from inertial wave resonances, the situation on Mars is different. The planet's tidal LOD variations have periods that are either too long or too far apart from those of inertial waves. Consequently, the associated contributions fall below the level of detectability.

1 Introduction

Thanks to the RISE (Rotation and Interior Structure Experiment) radio science experiment, part of NASA's InSight mission (Interior Exploration using Seismic Investigations, Geodesy, and Heat Transport), Mars' rotation and spatial orientation can now be determined with high precision. In particular, variations in the Length-of-Day (LOD) have been measured with an accuracy of 0.002 milliseconds (equivalent to 2 milliarcseconds (marcsec)), and nutations have been resolved to within a few marcsec (Le Maistre et al., 2023). The nutation data confirm that Mars' core is at least partially liquid.

The nutation of Mars is mainly induced by the Sun, since its moons Phobos and Deimos are very small, and their tidal effects remain weak (Baland et al., 2020). Consequently, the dominant nutation frequencies are the annual term and its sub-harmonics (semi-annual, ter-annual, quarter-annual, etc.). The amplitudes of the principal nutation components for the rigid-Mars nutation and the non-rigid contributions are shown in Fig. 1.

The annual term corresponds to one Martian year (about 1.88 Earth years, i.e., 687 d). Their amplitudes reach more than 500 marcsec in the prograde frequency band (positive periods in Fig. 1) and more than 130 marcsec in the retro-

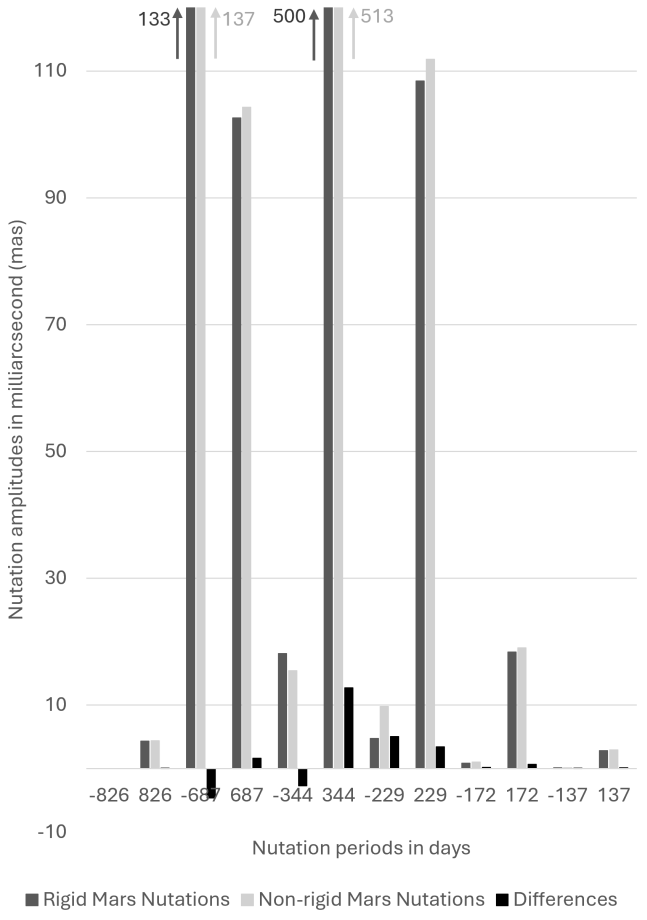

Figure 1. Amplitudes of the main nutations of Mars. Note that the two largest ones have their amplitudes truncated for the sake of visualization. Negative periods correspond to retrograde nutations and positive, to prograde nutations.

grade frequency band (negative periods in Fig. 1). These nutations are particularly valuable because they provide constraints on the interior structure of Mars, especially the size and state of its core (Dehant et al., 2000, 2009, 2011, 2012; Le Maistre et al., 2023). In addition, a nutation of about 5 marcsec amplitude with a period of 826 d has been identified, arising from a combination of terms involving both the orbital period of Phobos and the orbital motion of Mars. Note that the InSight nutation observations of Mars have not revealed the presence of a free mode, unlike for Earth (free FCN – Free Core Nutation at 430 d).

Seasonal variations in Mars' length of day (LOD) are substantial because a significant fraction of the atmosphere – about one quarter – participates in the sublimation and condensation cycle at the polar ice caps. Remarkably, these variations are comparable in magnitude to those on Earth, despite Mars having a much thinner atmosphere.

The internal structure of the Martian mantle has been inferred from seismic data (Banerdt et al., 2020; Drilleau et al., 2021, 2024; Stähler et al., 2021; Khan et al., 2021; Samuel et al., 2023) and spacecraft-derived gravity field measurements (e.g., Smith et al., 1999; Konopliv et al., 2016). These observations provide evidence for subsurface mass anomalies, associated viscous relaxation, and dynamic topography – i.e., topography at the core-mantle boundary caused by flow and pressure from mantle convection, which reflects and sustains the mantle's internal structure (Wieczorek, 2015). Recently, Charalambous et al. (2025) presented evidence for kilometre-scale heterogeneities throughout Mars' mantle using seismic data from InSight. Kiefer et al. (1996) used long-wavelength topographic and gravity data to infer the mantle's thermal structure, revealing the presence of deep-seated anomalies. Their results highlight dominant contributions from spherical harmonic degrees 2 and 3. As evident from any global image of Mars, and particularly from altimetry data, the northern hemisphere is lower than the southern hemisphere – a characteristic known as the Martian dichotomy (Zuber et al., 2000). This dichotomy is quantified by the degree-1 coefficient of Mars' surface topography. This large-scale hemispheric asymmetry is clearly visible on Mars, which exhibits relatively young northern lowlands and heavily cratered, older southern highlands. Recently, Goossens and Sabaka (2025) examined the degree-1 gravity associated with dichotomy, also clearly mentioned in Wieczorek et al. (2019), although they noted that the current resolution is insufficient for a robust determination of the corresponding large-scale density variations. Another distinctive feature of Mars is the presence of the vast Tharsis volcanic province, which has undergone prolonged volcanic activity over an extended period (Wieczorek, 2015). Zuber and Smith (1997) attempted to "remove" Tharsis from the Martian gravitational field in order to isolate its specific contributions. In doing so, they identified Tharsis as contributing primarily to degree-2, orders 0 and 2, as well as to degree-3, orders 0 and 3 – although the latter components were found to be relatively small. Defraigne et al. (2001) proposed the presence of a mantle upwelling plume beneath Tharsis to explain the observed geoid anomaly. However, due to uncertainties in the observations, it remains impossible to discriminate between different mantle models that incorporate such a plume and its effects on core–mantle boundary (CMB) topography. In this study, we assume a solid viscous mantle overlying the liquid core and disregard the possible existence of a basal liquid layer in the mantle, as suggested by Khan et al. (2023). Seismic data indicate that the Martian core is unusually large (Stähler et al., 2021), a result corroborated by radioscience measurements (Le Maistre et al., 2023). With a core of this size, mantle pressures are insufficient to trigger a ringwoodite–bridgmanite phase transition in the lower mantle. Consequently, the predicted CMB topography, ranging from 1 km to 5 km, is greater than in cases with a post-spinel phase transition. The impact of deviation from hydrostatic equilibrium at degree 2–order 0 of that level on the FCN was already highlighted in Defraigne et al. (2001). These results have motivated us to investigate the effects of

CMB topography, expressed in spherical harmonics – particularly for degree-1, degree-2, and degree-3 – on the FCN, nutations, and LOD variations. Adding further interest to the liquid–solid boundary, Khan et al. (2023) and Samuel et al. (2023) recently showed that InSight data require the presence of a fully molten, ~ 150 km-thick silicate layer overlying the liquid iron core. While this explains seismic observations, it might complicate the determination of the FCN from the geodetic data. This issue is still under study.

For comparison, in the case of Earth, nutation observations as well as variations in the length of day (LOD) provide valuable constraints on the deep interior, and in particular on coupling mechanisms at the core–mantle boundary (CMB). For nutations, following an approach similar to that of Koot et al. (2010), we recently re-evaluated the coupling constants at both the CMB and the inner core boundary. The revised values allow for additional coupling mechanisms beyond viscous and electromagnetic coupling. The incorporation of updated atmospheric and oceanic corrections to the nutation data has led to the determination of a larger CMB coupling constant than that reported by Koot et al., thereby leaving more room for non-hydrostatic or topographic coupling (Cheng et al., 2026). In addition, the electromagnetic coupling strength estimated by Mathews et al. (2002; see also Buffet et al., 2002) is likely overestimated, since the skin depth of magnetic diffusion at diurnal timescales is smaller than the thickness of any plausible electrically conducting layer at the base of the mantle and the lower mantle conductivity might even be smaller than that of the core. Although turbulence could enhance the effective viscosity, it is unlikely to increase it by several orders of magnitude (Shih et al., 2023). Consequently, topographic coupling remains a viable mechanism to account for the observed nutation. However, as shown for the Earth (Puica et al., 2023; Dehant et al., 2025), the pressure torque acting on the CMB is proportional to the product of topography coefficients $\varepsilon_l^k \varepsilon_{l'}^{k'}$ when the topography is expressed in spherical harmonics and normalized by the core radius. It is therefore of second order in the topography, which additionally decreases with increasing degree of the spherical harmonics (Kaula's law, see Puica et al., 2023). The pressure torque can therefore be expected to be much smaller than the pressure torque associated with the hydrostatic flattening of the core ($(\varepsilon_2^0)_{\text{hydrostatic}}$), in particular for high spherical harmonic degrees l, as the topography amplitude decreases with increasing degree. Nevertheless, the expression of the torque involves functions of inertial wave frequencies, which can lead to resonance effects when the tidal forcing frequency approaches the inertial wave frequency. These inertial waves, governed by the restoring effect of the Coriolis force, have periods of the order of weekly, diurnal, or sub-diurnal cycles and experience limited damping. As a result, they are strong candidates for influencing nutations and short-period variations in LOD, provided a resonance effect occurs. This consideration has motivated us to analyse these cases through a spherical harmonic expansion of the topography up to degree 24, beyond which the topography amplitude becomes too small to affect observations, even near resonance.

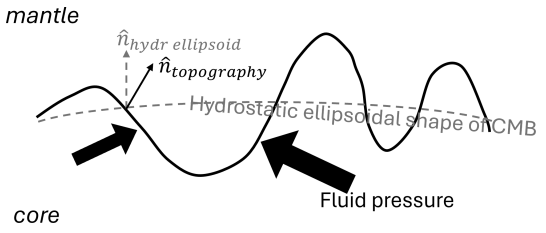

Figure 2. Representation of the pressure torque acting on the core-mantle boundary, where $\hat{n}_{\text{topography}}$ is the normal to the topography and $\hat{n}_{\text{hydr ellipsoid}}$ is the normal to the hydrostatic ellipsoid corresponding to the CMB.

In our papers published in 2023 (Puica et al.) and in 2025 (Dehant et al.), we reviewed the state-of-the-art and discussed the literature available at that time. Since then, in a recent paper, Monville et al. (2025) presented topography-coupling computations using local models of the CMB that incorporate rotation, buoyancy, and magnetic effects in a nonlinear regime. Due to the presence of both a magnetic field and stratification in the core, similarly as in the work of Seuren et al. (2026), their models include not only inertial waves but also Magneto-Archimedean-Coriolis (MAC) waves and Rossby waves. They compute the drag force exerted by core flows on the solid mantle and conclude that only large horizontal length scales contribute significantly to the CMB pressure torque. In our study, we focus exclusively on inertial waves (shorter timescale), as Mars currently lacks an active magnetic field. In addition, Guervilly and Dormy (2025) conclude that core convection in the absence of a magnetic field is dominated by the inertial scale, which is hundred times larger than the viscous scale. Note that these studies neglect turbulence. In parallel, Oliver et al. (2025) show that turbulence in Earth's core can generate large topographic torques on the mantle – an effect not considered in the present work. Similarly, Rekier et al. (2025) investigated the form-drag effect, which may provide a viable explanation for the observed CMB coupling constant (Koot et al., 2010; Cheng et al., 2026).

To set the stage, we examine here the variations in Mars' orientation and rotation that could potentially be induced by the pressure torque acting on the topography at the core–mantle boundary (CMB) (see Fig. 2).

In the presence of a rapidly rotating liquid core, inertial waves may develop within the core if suitably excited. These waves are oscillatory motions of fluid primarily controlled by rotation, rather than by buoyancy or elasticity. They propagate along characteristic directions inclined with respect to the rotation axis. For specific geometrical configurations, inertial waves can form global resonant modes within the core. At particular latitudes – known as critical latitudes – the

wave characteristics become tangent to the boundary, leading to locally amplified velocities and the generation of internal shear layers that propagate into the fluid interior. If present, such motions could influence the planet's orientation and rotational dynamics. Topography at the CMB may provide a mechanism for exciting these waves. In this paper, we compute the pressure effects exerted on the topography using an analytical approach to determine the torque applied to the CMB. The general expression for this torque is presented in Sect. 2. We examine the impact on nutations in Sect. 3 and on LOD variations in Sect. 4. More precisely, *in Sect. 3*, we derive the analytical expression for the dynamic pressure amplitude, expanded in spherical harmonics, by considering the CMB flow boundary conditions (Sect. 3.1). The corresponding torque, also expressed analytically, depends on the topography coefficients developed in spherical harmonics (Sect. 3.2). The nutation amplitudes are then derived from the coupling constant associated with this torque (Sect. 3.3). We compare our results with those obtained for Earth in a recent study (Dehant et al., 2025) in the appendix of this paper. *In Sect. 4*, we analyse the LOD case, which is more straightforward, as the analytical expression for pressure takes a simpler form. We also compare our findings with those for Earth, as presented in a recent study by Puica et al. (2023) (see Appendix). Finally, in Sect. 5, we present our conclusions.

2 Expression of the pressure torque on a bumpy core-mantle boundary

In the context of modelling Mars' orientation and rotational dynamics, the Liouville equations, which describe the conservation of angular momentum, form the theoretical foundation for quantifying how external torques – such as those from the atmosphere or solar tides – and internal torques between core and mantle affect the planet's spin axis orientation – nutations – and length-of-day variations (Wu and Wahr, 1997; Puica et al., 2023; Dehant et al., 2025). The presence of a pressure torque at the bumpy core-mantle boundary (CMB), $\mathbf{\Gamma^{topo}}$, introduces an additional term in the Liouville equations – beyond the pressure contribution due to the core's hydrostatic flattening ($(\varepsilon_2^0)_{\text{hydrostatic}}$). To quantify this torque, the CMB radius is represented using a spherical harmonic expansion:

$$r_{\text{CMB}} = R\Bigg[1 + \varepsilon_0^0 + (\varepsilon_2^0)_{\text{hydrostatic}} P_2^0(\cos\theta) + \sum_{n=1}^{\infty}\sum_{m=-n}^{n} \varepsilon_n^m Y_n^m(\theta,\lambda)\Bigg] \tag{1}$$

where ε_n^m are the normalized coefficients of the CMB topography expansion, R is the mean CMB radius, and $Y_n^m(\theta,\lambda)$ are the fully normalized spherical harmonic functions, defined in terms of the fully normalized associated Legendre functions P_n^m by

$$Y_n^m(\theta,\lambda) = P_n^m(\cos\theta)\, e^{im\lambda} \tag{2}$$

with (θ,λ) representing colatitude and longitude. Following Wu and Wahr (1997), we express the normalized dynamic pressure Φ as:

$$\Phi = \sum_{l=1}^{l_{\max}} a_l^k P_l^k\left(\frac{\sigma}{2}\right) Y_l^k(\theta,\lambda) \tag{3}$$

where σ is the frequency in a mantle-fixed reference frame, and the coefficients a_l^k are determined by using the boundary conditions that relate the Poincaré motion (the main flow for nutations) or the global core faster or slower rotation with respect to the mantle (the main flow for LOD tidal effects) to the inertial waves. In our previous work for the Earth (Puica et al., 2023, for LOD; Dehant et al., 2025, for nutations), we employed a fully analytical approach, in contrast to Wu and Wahr (1997), who used a semi-analytical method.

For the nutation case, we consider the x- and y-components of the torque $\mathbf{\Gamma^{topo}}$ (Γ_1^{topo} and Γ_2^{topo}, respectively) on the diurnal timescale. For Length-of-Day (LOD) variations, we focus on the z-component of the torque (Γ_3^{topo}). The equatorial torque components can be expressed as (Dehant et al., 2025)

$$\begin{aligned}\Gamma_1^{\text{topo}} &= \left(-iA_f\Omega^2\right)\left(\frac{15}{8\pi}\right) \\ &\times\frac{1}{2}\sum_{l=1}^{\infty}\sum_{k=-l}^{l}(-1)^k\Big[\sqrt{l-k}\sqrt{l+k+1}\,\varepsilon_l^{-k-1} \\ &+\sqrt{l-k+1}\sqrt{l+k}\,\varepsilon_l^{-k+1}\Big]P_l^k\left(\frac{\sigma}{2}\right)a_l^k\end{aligned} \tag{4}$$

$$\begin{aligned}\Gamma_2^{\text{topo}} &= \left(A_f\Omega^2\right)\left(\frac{15}{8\pi}\right) \\ &\times\frac{1}{2}\sum_{l=1}^{\infty}\sum_{k=-l}^{l}(-1)^k\Big[-\sqrt{l-k}\sqrt{l+k+1}\,\varepsilon_l^{-k-1} \\ &+\sqrt{l-k+1}\sqrt{l+k}\,\varepsilon_l^{-k+1}\Big]P_l^k\left(\frac{\sigma}{2}\right)a_l^k\end{aligned} \tag{5}$$

or in a complex form as

$$\begin{aligned}\tilde{\Gamma}_{\text{topo}}(\sigma) &= \Gamma_1^{\text{topo}} + i\Gamma_2^{\text{topo}} \\ &= \left(-iA_f\Omega^2\right)\left(\frac{15}{8\pi}\right) \\ &\times\sum_{l=1}^{\infty}\sum_{k=-l}^{l}(-1)^k\Big[\sqrt{l-k}\sqrt{l+k+1}\,\varepsilon_l^{-k-1}\Big] \\ &\times P_l^k\left(\frac{\sigma}{2}\right)a_l^k\end{aligned} \tag{6}$$

The polar component can be expressed as (Puica et al., 2023)

$$\begin{aligned}\Gamma_3^{\text{topo}} &= \left(iA_f\Omega^2\right)\left(\frac{15}{8\pi}\right) \\ &\times\frac{1}{2}\sum_{l=1}^{\infty}\sum_{k=-l}^{l}(-1)^k k\,\varepsilon_l^{-k}P_l^k\left(\frac{\sigma}{2}\right)a_l^k\end{aligned} \tag{7}$$

In these expressions, A_f is the mean core moment of inertia and Ω is the planet mean rotation frequency. The factor $\frac{15}{8\pi}$

is coming from the definition of Wu and Wahr of the torque, involving $\rho_f \Omega^2 R^5$ where ρ_f is the core density.

In Eq. (6), the coefficients a_l^k are substituted by using boundary conditions that relate the Poincaré motion ($\boldsymbol{\omega_f} \times \boldsymbol{r}$) – where $\boldsymbol{r}$ denotes the position vector of a fluid particle and $\boldsymbol{\omega_f}$ represents the vectorial wobble of the core relative to the mantle (Sasao et al., 1980) – to the inertial waves induced by the bumpy core-mantle boundary (Greenspan, 1969). In Eq. (7), the coefficients a_l^k are substituted using the boundary conditions corresponding to the global core rotation relative to the mantle, with $\omega_{f3} = -\omega_3$, where ω_3 is the third (axial) component of the mantle's rotation. These boundary conditions are described in detail in the Appendices A and B of Wu and Wahr (1997). Since the torque components (Eqs. 6 and 7) are proportional to either $\varepsilon_l^{-k-1} a_l^k$ or $\varepsilon_l^{-k} a_l^k$, and the coefficients a_l^k themselves are proportional to the topography, the torque components exhibit a quadratic dependence on the topography.

3 Nutation case

3.1 Boundary conditions

In the nutation case, to first order in ε_n^m, the relevant boundary conditions (Wu and Wahr, 1997) involve the mantle wobble with a normalized amplitude m, the Poincaré wobble in the core, with a normalized amplitude m_f, as well as inertial waves of which the expression in spherical harmonics includes the coefficients a_l^k.

At first order, and in the absence of topography, the ratio between mantle and core wobble amplitudes is given by:

$$\frac{m}{m_f} = \frac{A_f}{A} \frac{\sigma_{\mathrm{FCN}} + \Omega}{\sigma_{\mathrm{FCN}} - \alpha\Omega} \approx \frac{A_f}{A} \sigma'_{\mathrm{FCN}} \tag{8}$$

where σ_{FCN} and σ'_{FCN} are the FCN frequencies expressed in the mantle frame and inertial space, respectively. Here, α denotes the dynamic flattening of the planet and A is the mean moment of inertia of the entire planet. This relation shows that m is approximatively three orders of magnitude smaller than m_f and can be neglected in the boundary conditions. As shown in Dehant et al. (2025, see their Eq. 17), the boundary condition can then be expressed at the first order as

$$\begin{aligned}
&\frac{2}{3}\left(\frac{\sqrt{4\pi}}{\sqrt{5}} Y_2^0 - 1\right) \sum\nolimits_{l,k} [\ldots]_l^k a_l^k Y_l^k \\
&= \left(-\frac{2}{3}\frac{\sqrt{4\pi}}{\sqrt{5}} Y_2^0\right) \left[\sqrt{\frac{2\pi}{15}} \left(1 Y_0^0 + 3 \sum\nolimits_{n=1} \varepsilon_n^m Y_n^m\right)\right. \\
&\quad \times \left(\frac{\sigma^2+\sigma-2}{\sigma} Y_2^1 m_f^- + \frac{-\sigma^2+\sigma+2}{\sigma} Y_2^{-1} m_f^+\right) \\
&\left. + \sqrt{\frac{2\pi}{3}} \left(\frac{\sigma^2+\sigma-2}{\sigma} Y_1^1 m_f^- + \frac{-\sigma^2+\sigma+2}{\sigma} Y_1^{-1} m_f^+\right) \Psi\right] \\
&+ \frac{2}{3}\sqrt{\frac{2\pi}{15}} \left(1 Y_0^0 + 3 \sum\nolimits_{n=1} \varepsilon_n^m Y_n^m\right) \\
&\quad \times \left(\frac{\sigma^2+\sigma-2}{\sigma} Y_2^1 m_f^- + \frac{-\sigma^2+\sigma+2}{\sigma} Y_2^{-1} m_f^+\right) \\
&+ \sqrt{\frac{2\pi}{15}} \left(\frac{\sigma+2}{2} Y_2^1 m_f^- + \frac{\sigma-2}{2} Y_2^{-1} m_f^+\right) \sum\nolimits_{n=1} m \varepsilon_n^m Y_n^m \\
&+ \sqrt{\frac{2\pi}{3}} \left(\frac{\sigma^2-2\sigma-8}{6\sigma} Y_1^1 m_f^- \right. \\
&\qquad \left. + \frac{-\sigma^2-2\sigma+8}{6\sigma} Y_1^{-1} m_f^+\right) \Psi
\end{aligned} \tag{9}$$

with

$$\begin{aligned}
\Psi = \sum\nolimits_{n=1}^{\infty} \sum\nolimits_{m=-n}^{n} \varepsilon_n^m \left[\frac{n\sqrt{n-m+1}\sqrt{n+m+1}}{\sqrt{2n+1}\sqrt{2n+3}} Y_{n+1}^m \right. \\
\left. - \frac{(n+1)\sqrt{n-m}\sqrt{n+m}}{\sqrt{2n+1}\sqrt{2n-1}} Y_{n-1}^m\right]
\end{aligned} \tag{10}$$

and

$$[\ldots]_l^k = \left[k P_l^k\left(\frac{\sigma}{2}\right) - \left(\frac{4-\sigma^2}{4}\right) P'^k_l\left(\frac{\sigma}{2}\right)\right] \tag{11}$$

Here, m_f^+ denotes the complex sum of the first two components of the normalized core wobble, while m_f^- represents their complex difference. Additionally, we have replaced $\sin^2\theta$ using the identity

$$\sin^2\theta = \frac{2}{3}\left(-\frac{\sqrt{4\pi}}{\sqrt{5}} Y_2^0 + 1\right) \tag{12}$$

In the above equations, the dimensionless frequency σ, expressed in cycles per day, is related to the nutation frequency σ'_n defined in inertial space and σ_n defined in a frame tied to the planet, by:

$$\sigma = 1 - \frac{\sigma'_n}{\Omega} = -\sigma_n \tag{13}$$

Note that while a negative quasi-diurnal frequency would typically be used in the selected reference frame, we follow

the convention of Wu and Wahr (1997) and adopt the opposite sign.

To solve Eq. (9), we begin by expanding the sums and products in the equation using properties of spherical harmonic, which involves Wigner symbols. We then project the resulting expressions onto a single spherical harmonic by multiplying by its complex conjugate and integrating over the sphere. Each projection results in an equation in which the right-hand side (RHS) contains combinations of topography coefficients $\varepsilon_l^{k\pm1}$, $\varepsilon_{l\pm2}^{k\pm1}$, and $\varepsilon_{l\pm4}^{k\pm1}$, while the left-hand side (LHS) consists of terms involving a_l^k and $a_{l\pm2}^k$. All these projections form a system of equation of the form

$$\mathbf{A_{nut}}\left(a_l^k\right) = f\left(\varepsilon_l^{k\pm1}, \varepsilon_{l\pm2}^{k\pm1}, \varepsilon_{l\pm4}^{k\pm1}\right) \tag{14}$$

Equation (14) can be resolved for the coefficients a_l^k by inverting the matrix $\mathbf{A_{nut}}$ on the LHS. In practice, however, the problem is more efficiently handled by partitioning the system of linear equations into multiple independent subsystems, each of which can be solved individually. However, for specific values of the frequency, the determinant of the matrix $\mathbf{A_{nut}}$ (or of the matrices of the subsystems) may be null, indicating singularities corresponding to *resonances*. Although Mars has a different uniform rotation rate, the resonances determined for the Earth (Dehant et al., 2025, Table 2) can still be used as a reference framework considering they are normalized by the Martian rotation Ω.

The impact on nutation of a given resonance depends on how closely its period aligns with the nutation periods of interest. We have summarized the approach in a sketch presented in Fig. 3.

For Mars, we have identified three such possible resonance cases involving the primary nutations and no case for LOD.

3.1.1 Degree 2

Since we primarily focus on low degrees (providing the largest topography amplitudes), we first consider the degree-2 topography coefficients only. Equation (14) then simplifies to 10 equations containing products of two or three spherical harmonics ($Y_2^{\pm2}Y_2^{\pm1}$, $Y_3^{\pm2}Y_1^{\pm1}$, $Y_2^0Y_2^{\pm2}Y_2^{\pm1}$, $Y_2^0Y_3^{\pm2}Y_1^{\pm1}$). Through the expression of a product of two spherical harmonics of degrees l_1 and l_2, and orders m_1 and m_2, as a sum of spherical harmonics with degrees ranging from $|l_1 - l_2|$ to $l_1 + l_2$, and orders $m_1 + m_2$ (see, for example, MacRobert, 1967), we obtain a sum involving the following spherical harmonics Y_2^1, Y_2^{-1}, Y_4^1, Y_4^{-1}, Y_4^3, Y_4^{-3}, Y_6^1, Y_6^{-1}, Y_6^3, Y_6^{-3}. The solutions of the 10 equations can be obtained by solving the four decoupled subsystems. Two involving degrees 4 and 6 with either order 3 or -3, and two with degrees 2, 4, and 6 with either order 1 or -1. The solutions of these subsystems can be expressed as

$$\begin{pmatrix} a_2^1 \\ a_4^1 \\ a_6^1 \end{pmatrix} = \begin{pmatrix} \frac{-1}{14[\ldots]_2^1}\left(\frac{3\sigma^2+4\sigma-20}{\sigma}\right) \\ \frac{5\sqrt{6}}{42[\ldots]_4^1}\left(\frac{\sigma^2-\sigma-2}{\sigma}\right) \\ 0 \end{pmatrix} \varepsilon_2^2 m_f^+ + \begin{pmatrix} \frac{-\sqrt{6}}{28[\ldots]_2^1}\left(\frac{\sigma^2+8\sigma+12}{\sigma}\right) \\ \frac{5}{7[\ldots]_4^1}\left(\frac{-\sigma^2-\sigma+2}{\sigma}\right) \\ 0 \end{pmatrix} \varepsilon_2^0 m_f^- \tag{15a}$$

$$\begin{pmatrix} a_2^{-1} \\ a_4^{-1} \\ a_6^{-1} \end{pmatrix} = \begin{pmatrix} \frac{1}{14[\ldots]_2^{-1}}\left(\frac{3\sigma^2-4\sigma-20}{\sigma}\right) \\ \frac{-5\sqrt{6}}{42[\ldots]_4^{-1}}\left(\frac{\sigma^2+\sigma-2}{\sigma}\right) \\ 0 \end{pmatrix} \varepsilon_2^{-2} m_f^- + \begin{pmatrix} \frac{\sqrt{6}}{28[\ldots]_2^{-1}}\left(\frac{\sigma^2-8\sigma+12}{\sigma}\right) \\ \frac{5}{7[\ldots]_4^{-1}}\left(\frac{\sigma^2-\sigma-2}{\sigma}\right) \\ 0 \end{pmatrix} \varepsilon_2^0 m_f^+ \tag{15b}$$

$$\begin{pmatrix} a_4^3 \\ a_6^3 \end{pmatrix} = \begin{pmatrix} \frac{-5}{\sqrt{42}[\ldots]_4^3}\left(\frac{\sigma^2+\sigma-2}{\sigma}\right) \\ 0 \end{pmatrix} \varepsilon_2^2 m_f^- \tag{15c}$$

$$\begin{pmatrix} a_4^{-3} \\ a_6^{-3} \end{pmatrix} = \begin{pmatrix} \frac{-5}{\sqrt{42}[\ldots]_4^{-3}}\left(\frac{-\sigma^2+\sigma+2}{\sigma}\right) \\ 0 \end{pmatrix} \varepsilon_2^{-2} m_f^+ \tag{15d}$$

They show that, for each frequency, the a_l^k coefficients depend only on the degree-2, order-0 or ±2 components of the topography, as well as on the position of the core rotation axis relative to the mantle (denoted $m_f^{\pm}$). These coefficients exhibit resonances at frequencies corresponding to the zeros of the bracketed terms appearing in the denominators of the governing Eqs. (15). These frequencies are at -2, -1.708, -1, -0.820, -0.612, -0.5, 0, 0.5, 0.612, 0.820, 1, 1.708, 2. Because nutations appear at diurnal frequencies in a frame tied to the planet (and following our convention, Eq. 13), only the frequency of $0.820\,\mathrm{cycles\,d^{-1}}$ in the Martian reference frame, corresponding to a period of about 5.5 d in space, could affect the nutations if resonant terms existed near that period. However, there is no nutation near that period (see Baland et al., 2020).

3.1.2 Degree 1

In the case of degree-1, we similarly get 13 solutions as follows:

$$a_1^0 = \frac{1}{[\ldots]_1^0}\left(\frac{\sqrt{2}}{210}\right)\left\{\frac{32\sigma^2+11\sigma-106}{\sigma}\varepsilon_1^{-1}m_f^- + \frac{-32\sigma^2+11\sigma+106}{\sigma}\varepsilon_1^1 m_f^+\right\} \tag{16a}$$

$$a_1^{\pm1} = \frac{1}{[\ldots]_1^{\pm1}}\left(\frac{-\sqrt{2}}{2}\right)\frac{\pm65\sigma^2+149\sigma\pm38}{210}\varepsilon_1^0 m_f^{-/+} \tag{16b}$$

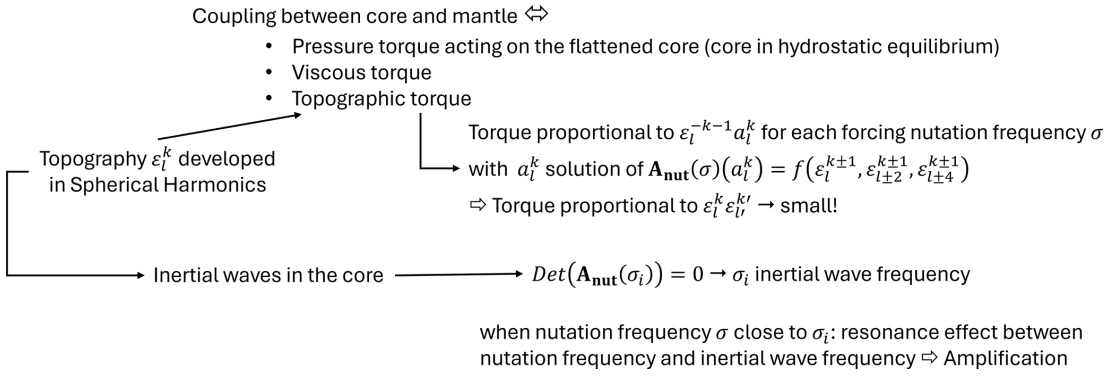

Figure 3. Sketch of the approach, showing the possible amplifications due to resonance effects with inertial modes.

$$a_3^0 = \frac{1}{[\ldots]_3^0}\left(\frac{-1}{5\sqrt{7}\sqrt{6}}\right)\left\{\frac{10\sigma^2+7\sigma-26}{\sigma}\varepsilon_1^{-1}m_f^- + \frac{-10\sigma^2+7\sigma+26}{\sigma}\varepsilon_1^1 m_f^+\right\} \quad (16c)$$

$$a_3^{\pm1} = \frac{1}{[\ldots]_3^{\pm1}}\left(\frac{-1}{30\sqrt{7}}\right)\left\{\frac{\pm35\sigma^2+29\sigma\pm(-82)}{\sigma}\right\} \times \varepsilon_1^0 m_f^{-/+} \quad (16d)$$

$$a_3^{\pm2} = \frac{1}{[\ldots]_3^{\pm2}}\frac{-11}{3\sqrt{7}\sqrt{5}}\left\{\frac{\pm\sigma^2+\sigma\pm(-2)}{\sigma}\right\}\varepsilon_1^1 m_f^{-/+} \quad (16e)$$

$$a_5^0 = \frac{1}{[\ldots]_5^0}\left(\frac{4}{7\sqrt{11}\sqrt{6}}\right)\left\{\frac{\sigma^2+\sigma-2}{\sigma}\varepsilon_1^{-1}m_f^- + \frac{-\sigma^2+\sigma+2}{\sigma}\varepsilon_1^1 m_f^+\right\} \quad (16f)$$

$$a_5^{\pm1} = \frac{1}{[\ldots]_5^1}\left(\frac{4\sqrt{2}}{7\sqrt{5}\sqrt{11}}\right)\frac{\pm\sigma^2+\sigma\pm(-2)}{\sigma}\varepsilon_1^0 m_f^{-/+} \quad (16g)$$

$$a_5^{\pm2} = \frac{1}{[\ldots]_5^{\pm2}}\frac{2}{\sqrt{5}\sqrt{7}\sqrt{11}}\frac{\pm\sigma^2+\sigma\pm(-2)}{\sigma}\varepsilon_1^1 m_f^{-/+} \quad (16h)$$

The a_l^k coefficients depend on the three degree-one topography coefficients and on the orientation of the rotation axis of the core. Here again, they exhibit resonances at frequencies corresponding to the zeros of the bracketed terms appearing in the denominators of the governing Eqs. (16). These frequencies are at −2, −1.806, −1.530, −1.510, −1.496, −1.183, −1.046, −0.894, −0.763, −0.667, −0.570, −0.467, −0.177, −0.068, 0, 0.068, 0.177, 0.467, 0.570, 0.667, 0.763, 0.894, 1.046, 1.183, 1.496, 1.510, 1.530, 1.806, 2. Only the frequencies 0.894, 1.046, 1.183 cycles d^{-1} in the Martian frame, corresponding to periods near 9.4 d, −21.7 d, and −5.5 d in space, could have an effect on the nutations. There is no nutation near these periods.

3.1.3 Other degrees

Also in the general case, the solutions for $a_l^{\pm k}$ exhibit resonances, determined by the roots of the corresponding $[\ldots]_l^{\pm k}$. Table 1 presents the inertial wave period (column 5), along with the degree l and order k of the spherical harmonics component of the topography generating them (column 4), as well as the potential nearby nutation period (columns 1, 2, and 3). The table also provides the difference, in days, between the nutation period and the inertial wave period (column 6).

Table 1 shows that the nutation closest to an inertial wave is the quarter-annual nutation, which is 1.4 d away from an inertial wave period (shown in bold in the Table 1).

3.2 Expression of the torque at the core-mantle boundary

The torque associated with the topography $\tilde{\Gamma}_{\mathrm{topo}}(\sigma)$ is expressed by Eqs. (4), (5), and (6) proportional to ε_l^{-k-1} or ε_l^{-k} and involving the normalized inertial pressure, Φ provided by Eq. (3), acting on the boundary bumps, which involves the normal to the CMB topography, as explained above in Sect. 2. As done in Dehant et al. (2025), we just need to substitute a_l^k as a function of ε_n^m (except for degree 2, order 1, as it corresponds to the first order torque on the ellipsoidal shape) to obtain the final expression of the torque.

For the topography coefficients ε_n^m, we adopt a generalized Kaula law, as supported by Puica et al. (2023). With this assumption, the CMB topography coefficients decrease with increasing spherical harmonic degree. The dominant contributions to $\tilde{\Gamma}_{\mathrm{topo}}(\sigma)$ on Mars are likely associated with dynamic topography driven by the mantle's internal structure, which is also reflected in surface gravity anomalies. As shown in Defraigne et al. (2001), the effect of mantle mass anomalies differs between the geoid and the CMB topography: the low-degree geoid is most sensitive to anomalies at depths of about 700 km, whereas the CMB topography is primarily sensitive to anomalies near the CMB, at approximately 1830 km depth. This relationship is encapsulated by

Table 1. Principal resonances close to Martian nutations.

Nutation period in Martian days	Nutation period in Martian year		Degree and order (l, k)	Inertial wave period in days	Difference between nutation period and inertial wave period in day
−111.430	1/6 year	retrograde	(12, 6)	−102.493	8.937
−111.430	1/6 year	retrograde	(24, −4)	−109.392	2.038
−167.150	1/4 year	retrograde	(18, −12)	−157.218	9.932
−222.866	1/3 year	retrograde	(12, −2)	−206.826	16.040
−334.300	0,5 year	retrograde	(16, −5)	−262.304	71.996
133.720	1/5 year	prograde	(21, −2)	135.876	2.156
133.720	1/5 year	prograde	(21, 6)	138.412	4.692
133.720	1/5 year	prograde	(24, −2)	125.853	7.867
133.720	1/5 year	prograde	(24, 6)	126.088	7.632
133.720	1/5 year	prograde	(23, −8)	148.036	14.316
167.150	1/4 year	prograde	(14, −6)	163.739	3.411
167.150	1/4 year	prograde	(23, −8)	148.036	19.114
167.150	1/4 year	prograde	(18, −2)	168.602	**1.453**
167.150	1/4 year	prograde	(18, 6)	182.895	15.745
167.150	1/4 year	prograde	(19, 9)	171.142	3.992
334.300	0,5 year	prograde	(21, 13)	274.074	60.226
334.300	0,5 year	prograde	(15, −2)	370.692	36.393
668.599	1 year	prograde	(15, 6)	793.770	125.171
668.599	1 year	prograde	(20, 15)	937.350	268.751
668.599	1 year	prograde	(23, 12)	1004.721	336.121

the Green's function – i.e., the kernel that links mantle mass anomalies to surface/geoid or CMB topography – derived in Defraigne et al. (2001). Using the observed geoid together with these Green's functions, and assuming that the amplitudes of mantle loads is independent of depth (but varies with the degree and order of each gravity coefficient), we can estimate the order of magnitude of the corresponding CMB topography. The viscosity profiles used in these computations are those proposed by Sohl and Spohn (1997) and adopted by Defraigne et al. (2001). Recent viscosity estimates from Broquet et al. (2025) are in very good agreement with these values. Although Defraigne et al. (2001) examined several alternative models, including cases with a bridgmanite layer at the base of the mantle, we restrict our analysis to models without such a layer and assume a large core, consistent with Le Maistre et al. (2023). In this framework, uncertainties in the viscosity profile affect the inferred CMB topography amplitude by no more than about 25 %. Under these assumptions, the topography amplitudes scale with the Martian gravity field coefficients, all listed in Table 2. Note that, for comparison, if Mars were in hydrostatic equilibrium, the difference between the equatorial and polar radii of the core would be on the order of 6 km.

The chosen CMB topography includes in fact a contribution from the Tharsis mass anomaly, which is predominantly represented by degree-2, order-2 terms, followed by degree-2, order-0, and then degree-3, order-3 components, in decreasing order of amplitude. As shown in Table 2, the degree-2 terms are the most significant (in bold in Table 2). Other components (such as ε_3^0, ε_3^{-1}, ε_3^1, ε_3^{-2}, ε_3^2, ε_4^{-4} and ε_4^4) are smaller than the degree-2 terms. Due to Mars' hemispheric dichotomy, the topography may also contain a significant degree-1 component, which we will account for in the following analysis. For that case, we use the computations of Wieczorek et al. (2019), who considered gravity anomalies within the lithosphere that perturb the shapes of the underlying hydrostatic density interfaces, including the core–mantle boundary.

3.2.1 Degree 2

For the a_l^k involving degree-2 spherical harmonics, the torque expression Eq. (1) yields:

$$\begin{aligned}\tilde{\Gamma}^{\text{topo}} &= \Gamma_1^{\text{topo}} + i\Gamma_2^{\text{topo}} \\ &= \left(-iA\Omega^2\right)\left(\frac{15}{8\pi}\right)\left\{\varepsilon_2^0 P_2^{-1}\left(\frac{\sigma}{2}\right)a_2^{-1}\right. \\ &+ \varepsilon_2^{-2} P_2^1\left(\frac{\sigma}{2}\right)a_2^1 + \varepsilon_4^0 P_4^{-1}\left(\frac{\sigma}{2}\right)a_4^{-1} \\ &\left.+ \varepsilon_4^{-2} P_4^1\left(\frac{\sigma}{2}\right)a_4^1\right\} \end{aligned} \tag{17}$$

Table 2. Main Mars gravity field coefficients.

Topography coefficients expressed as sine (s) and cosine (c) components relevant for Tharsis	Normalized Mars gravity field coefficients amplitudes (Zuber and Smith, 1997; Smith et al., 1993) (*10^{-6} and above 10^{-5})	Order of magnitude of the CMB topography contribution (m)
ε_2^0	**−44**	**400**
ε_{c2}^1 and ε_{s2}^1 (or equivalently ε_2^{-1} and ε_2^1)	0.004 and 0.007	
ε_{c2}^2 and ε_{s2}^2 (or equivalently ε_2^{-2} and ε_2^2)	**84** and **50**	**760** and **450**
ε_3^0	−12	250
ε_{c3}^1 and ε_{s3}^1 (or equivalently ε_3^{-1} and ε_3^1)	4 and 25	65 and 390
ε_{c3}^2 and ε_{s3}^2 (or equivalently ε_3^{-2} and ε_3^2)	16 and 8	250 and 125
ε_{c3}^3 and ε_{s3}^3 (or equivalently ε_3^{-3} and ε_3^3)	35 and 25	550 and 390
ε_{c4}^4 and ε_{s4}^4 (or equivalently ε_4^{-4} and ε_4^4)	0.1 and −13	2 and 330

After substituting Eqs. (15) for the a_l^k, we obtain:

$$\begin{aligned}\tilde{\Gamma}^{\text{topo}} = &\left(-iA\Omega^2\right)\left(\frac{15}{8\pi}\right)\left\{\frac{1}{16}\sigma(4-\sigma^2)^{1/2}\right.\\
&\times\left\{\frac{1}{14[\ldots]_2^{-1}}\left(\frac{3\sigma^2-4\sigma-20}{\sigma}\right)\varepsilon_2^0\varepsilon_2^{-2}m_f^-\right.\\
&\left.+\frac{\sqrt{6}}{28[\ldots]_2^{-1}}\left(\frac{\sigma^2-8\sigma+12}{\sigma}\right)\varepsilon_2^0\varepsilon_2^0m_f^+\right\}\\
&+\frac{-3}{8}\sigma(4-\sigma^2)^{1/2}\\
&\times\left\{\frac{-1}{14[\ldots]_2^{1}}\left(\frac{3\sigma^2+4\sigma-20}{\sigma}\right)\varepsilon_2^{-2}\varepsilon_2^2m_f^+\right.\\
&\left.+\frac{-\sqrt{6}}{28[\ldots]_2^{1}}\left(\frac{\sigma^2+8\sigma+12}{\sigma}\right)\varepsilon_2^0\varepsilon_2^{-2}m_f^-\right\}\\
&+\frac{1}{128}(7\sigma^3-12\sigma)(4-\sigma^2)^{1/2}\\
&\times\left\{\frac{-5\sqrt{6}}{42[\ldots]_4^{-1}}\left(\frac{\sigma^2+\sigma-2}{\sigma}\right)\varepsilon_4^0\varepsilon_2^2m_f^+\right.\\
&\left.+\frac{5}{7[\ldots]_4^{-1}}\left(\frac{\sigma^2-\sigma-2}{\sigma}\right)\varepsilon_4^0\varepsilon_2^0m_f^+\right\}\\
&+\frac{-5}{32}(7\sigma^3-12\sigma)(4-\sigma^2)^{1/2}\\
&\times\left\{\frac{5\sqrt{6}}{42[\ldots]_4^{1}}\left(\frac{\sigma^2-\sigma-2}{\sigma}\right)\varepsilon_4^{-2}\varepsilon_2^2m_f^+\right.\\
&\left.\left.+\frac{5}{7[\ldots]_4^{1}}\left(\frac{-\sigma^2-\sigma+2}{\sigma}\right)\varepsilon_4^2\varepsilon_2^0m_f^+\right\}\right\} \qquad (18)\end{aligned}$$

where the brackets $[\ldots]_{2/4}^{\pm1}$ are obtained from Eq. (11).

3.2.2 Degree 1

For the a_l^k involving degree-1 spherical harmonics the torque expression Eq. (6) can be expressed considering the topographic coefficients relevant to both the dichotomy and Tharsis, and substituting the expressions for P_l^k and a_l^k, involving $[\ldots]_l^k$:

$$\begin{aligned}\tilde{\Gamma}^{\text{topo}} = \Gamma_1^{\text{topo}} + i\Gamma_2^{\text{topo}} = &\left(-iA\Omega^2\right)\left(\frac{15}{8\pi}\right)\\
&\times\left\{\left(\frac{-1}{210}\right)\frac{65\sigma^2+149\sigma+38}{\sigma-2}\varepsilon_1^0\varepsilon_1^0m_f^+\right.\\
&+\left(\frac{2}{105}\right)\frac{32\sigma^2+11\sigma-106}{\sigma^2-4}\varepsilon_1^{-1}m_f^-\\
&+\left(\frac{-2}{105}\right)\frac{32\sigma^2-11\sigma-106}{\sigma^2-4}\varepsilon_1^1m_f^+\\
&\left.+\left(\frac{-22\sqrt{2}}{\sqrt{7}\sqrt{15}}\right)\frac{\sigma^2+\sigma-2}{3\sigma^2-4\sigma+4}\varepsilon_3^{-3}\varepsilon_1^{-1}m_f^+\right\} \qquad (19)\end{aligned}$$

where the roots of $\sigma-2$, σ^2-4, and $3\sigma^2-4\sigma+4$ provide resonances. Nothing appears in the nutation frequency band.

3.3 Effects on nutations

The transfer function for nutations can be derived from the transfer function for the mantle wobble $\tilde{m}$ of Mars defined as the complex sum of the two first components of the non-dimensional rotation axis coordinates $(m_1 + i\,m_2)$. The wobbles, $\tilde{m}$ and $\tilde{m}_f$, of the mantle and the core (with $\tilde{m}_f = m_{f1} + i\,m_{f2}$), respectively, are solutions to the Liouville equations. We distinguish between the case without topography (denoted as $\tilde{m}^0$ and $\tilde{m}_f^0$), and the case with a topography at the CMB. The additional contribution to the mantle wobble due to the topography (Dehant et al., 2025) is proportional to the topographic torque, as computed in the previous

section or in Sect. 2 (Eq. 6), according to

$$\tilde{m} = \tilde{m}^0 - i\frac{\sigma_n}{\sigma_n - \sigma_{n\mathrm{FCN}}}\frac{\tilde{\Gamma}_{\mathrm{topo}}}{A_m \Omega^2} \tag{20}$$

where σ_n is the nutation frequency as introduced above (Eq. 13), $\sigma_{n\mathrm{FCN}}$ is the FCN frequency, and A_m is the mean mantle moment of inertia. The associated nutation contribution $\Delta\tilde{\eta}_n$ can be determined from the nutation transfer function given by Eq. (1) from Dehant et al. (2025):

$$\begin{aligned}\Delta\tilde{\eta}_n(\sigma_n) &= \tilde{\eta}_n - \tilde{\eta}_n^0 \\ &= \tilde{\eta}_n^0 \left(\frac{-\sigma_n}{\Omega_0 (\sigma_n - \sigma_{n\mathrm{FCN}})(A\sigma_n - A_m \sigma_{n\mathrm{FCN}})} \right. \\ &\left. \times \frac{A}{A_m} \frac{i\tilde{\Gamma}_{\mathrm{topo}}(\sigma)}{m_f^+(\sigma)} \right)\end{aligned} \tag{21}$$

where $\tilde{\eta}_n$ is the complex sum of the rotation pole first-two components expressing nutations in space and where the superscript 0 indicates the values when there is no topography. For the highest degrees, since the topographic torque depends on the square of the small topography coefficients, significant contributions can only occur in the vicinity of resonances. Figure 4 displays the determinant of the matrix $\mathbf{A_{nut}}$ in Eq. (14) (up to degree 24) to be inverted. Values equal to zero indicate the frequencies at which resonances can occur for nutations. The zero-crossings are thus the relevant quantities for identifying resonances; the vertical amplitude itself does not carry direct physical significance in this context. In this figure, nutations appear in the diurnal frequency band in a frame tied to the planet; retrograde long-period nutations in space appear thus at frequencies $\sigma > 1$; whereas prograde long-period nutations in space appear at frequencies $\sigma < 1$.

In Sect. 3.2.1, we have provided, as an example, the degree-2 contributions to the torque, where we observe some resonance effects when the nutation frequencies are close to the frequencies corresponding to brackets $[\ldots]^{\pm 1}_{2/4}$ close to 0. Figure 4 shows the results for all degrees. For the primary nutations of Mars, we have identified three possible resonances (see Table 1):

(1) **First resonance**: This occurs in the solution for a_{24}^{-4}, appearing at approximately −109.39 Martian d, close to the 1/6 year retrograde nutation at −111.43 Martian d. However, this nutation has a very small amplitude of 20 µarcsec (see Reasenberg and King, 1979; Baland et al., 2020), and the resonance is 2.0 Martian d away from it. As a result, the computed topography effect remains below the µarcsec level.

(2) **Second resonance**: This appears in the solution for a_{21}^{-2} at 135.88 Martian d, near the 1/5 year prograde nutation at 133.72 Martian d. In this case as well, the amplitude is very small at 2.8 marcsec, and the resonance is 2.1 d away from the nutation. Consequently, the effect remains well below the µarcsec level.

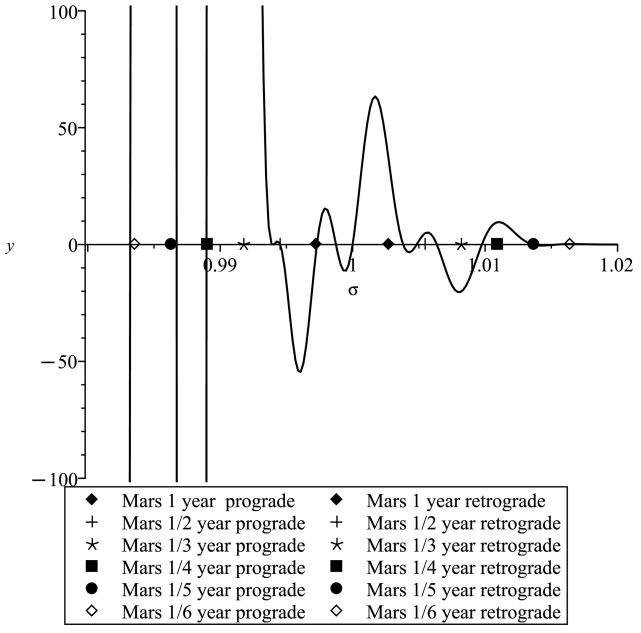

Figure 4. Determinant of the matrix $\mathbf{A_{nut}}$ involved in the system of Eqs. (14), showing the resonances where the curve is crossing zero. The x axis represents the frequencies in cycles d^{-1} in a frame tied to the planet. The nutation periods in that frame are shown in the diurnal frequency band with the symbols expressed in the legend on the left-hand side of 1 cycles d^{-1} for prograde nutations and on the right-hand-side of 1 cycles d^{-1} for the retrograde nutations.

(3) **Third resonance**: This occurs in the solution for a_{18}^{-2}, appearing at approximately 168.60 Martian d, close to the 1/4 year prograde nutation at 167.15 Martian d. While its amplitude is 18.4 marcsec, its period is still more than 1 d from the resonance, and the associated topography is extremely small (as for the two other cases), resulting in an effect at the µarcsec level.

In conclusion, the forced nutation frequencies are insufficiently close to any resonant frequency to have a significant effect on the nutation (not even at the µarcsec level).

4 Length-of-day variations

The effects of CMB topography on the tidal variations in Mars' LOD can be calculated using a similar approach to that described above (Puica et al., 2023, for the Earth). For LOD, and analogously to the boundary conditions for nutations (Eqs. 9 and 14), we have a system of equations of the form:

$$\mathbf{A_{LOD}}\left(a_l^k\right) = f\left(\varepsilon_l^k\right) \tag{22}$$

where each equation for a particular order l and degree k involves a bracket $[\ldots]_l^k$ on the LHS and a function of ε_l^k on the RHS. The solutions yield expressions for the coefficients

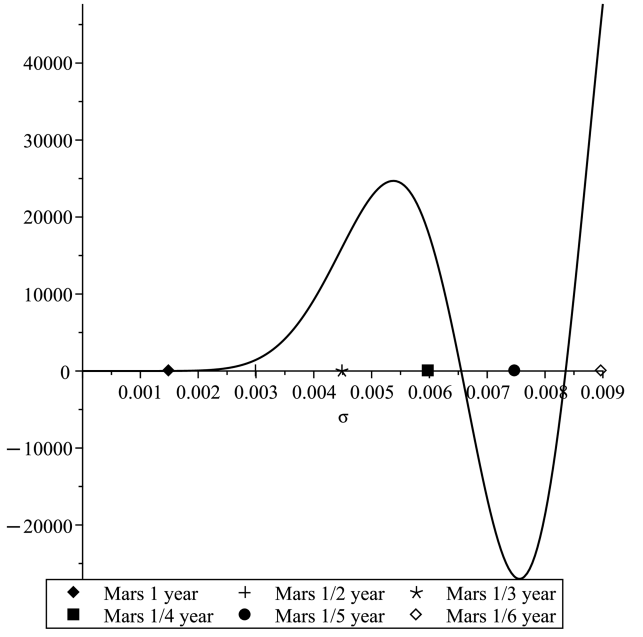

Figure 5. Determinant of the matrix $\mathbf{A_{LOD}}$ involved in the system of Eqs. (22), showing the resonances where the curve is crossing zero. The x axis represents the frequencies in cycles d^{-1}. The LOD seasonal periods are shown with the symbols expressed in the legend.

a_l^k given in Eq. (28) of Puica et al. (2023). The zeros of the determinant of the matrix $\mathbf{A_{LOD}}$, which correspond to the zeros of the $[\ldots]_l^k$ brackets, indicate resonance effects.

We then substitute the solution of Eq. (22) for a_l^k into the expression for the torque, which is in turn substituted into the expression of the tidal variations in LOD, $\Delta\mathrm{LOD}(\sigma)$. Finally, the LOD variations can be expressed as a function of the axial component of the mantle wobble, m_3:

$$\Delta\mathrm{LOD}(\sigma) = -i\frac{\Gamma_3}{A_m\sigma\Omega^2} = \frac{A_f}{A_m}\left(\frac{15}{8\pi}\right) \times \left(\sum_{l=1}^{l_{\max}}\sum_{k=-l}^{l}(-1)^k k^2 \varepsilon_l^k \varepsilon_l^{-k} P_l^k\left(\frac{\sigma}{2}\right)\frac{(4-\sigma^2)}{4\sigma[\ldots]_l^k} m_3\right) \tag{23}$$

where the product $\varepsilon_l^k\varepsilon_l^{-k}$ clearly shows the quadratic dependence of the LOD on the topography. Resonances occur only when the denominator term $[\ldots]_l^k = 0$. Figure 5 shows the determinant of the matrix $\mathbf{A_{LOD}}$. As in Fig. 4 (nutation case), the presence of resonances in LOD is indicated when the curve crosses the zero line on the x axis. The closer these crossing are with respect to the tidal periods involved in LOD (and referenced with the symbols given in the legend of the figure), the higher the resonance would be.

As shown in Fig. 5 there are no resonances close to the Martian tidal frequencies of 668.6, 334.3, 222.9, 167.15, 133.7, and 111.4 Martian d (shown with symbols explained in the legend). The nearest periods to a resonance (shown when the curve is crossing the 0-line on the x axis) are the 1/6 year (or 111.4 d) and 1/4 year (or 167.15 d) tides, which are approximately 7.9 and 4.4 d away from an inertial wave resonance (at 103.5 and 162.7 d), respectively. These distances are too large to produce significant resonant effects, particularly given that the associated spherical harmonic degrees (15 and 22) correspond to extremely small topographic coefficients (ε_{15}^{-1} and ε_{22}^{-2}). In contrast, for Earth, several tidal periods shorter than one month led to resonances near the 13.63 and 27.6 d tides (see Puica et al., 2023).

5 Conclusions

Following our previous studies on topographic effects on Earth's LOD and nutations – where potential resonance effects with inertial waves were demonstrated – we applied our analytical framework to planet Mars. The existence of core modes within Mars is plausible, as its core has been shown to be liquid. In the absence of a significant magnetic field, these modes are essentially inertial waves, with the Coriolis force acting as the primary restoring mechanism.

In our model, we considered primary a possible degree-1 topography related to Mars' hemispheric dichotomy, as well as low-degree topographic features potentially associated with the dynamic loading from the Tharsis region at the CMB. We also considered higher degree effects through a Kaula-law extrapolation of the topography.

Our analysis of Martian nutations reveals a potential resonance at 168.60 Martian d, which lies close to the 1/4 year prograde nutation period at 167.15 Martian d – differing by just over one day. This nutation exhibits an amplitude of 18.4 marcsec, which is significant at the level of radioscience observations. However, despite this proximity, the actual topography contribution to nutation remains negligible, as the resonance involves a high degree (degree-18) and therefore small topographic amplitude.

Unlike Earth, where LOD variations can be significantly influenced by low-degree CMB topography, Mars shows no comparable resonant effects near its tidal periods. As a result, we find no evidence of substantial inertial wave resonance contributing to LOD variations on Mars. Generally speaking, in our analytical case, we found a quadratic dependence on the topography amplitude, both for Earth and Mars. As a result, the effects of CMB coupling are generally small, unless resonances occur.

Our study does not consider the effect of turbulence at the CMB. Using numerical simulations of hydrodynamic convection in a rotating spherical shell with boundary topography, Oliver et al. (2025) recently showed that turbulent flow in the core of the Earth can lead to a pressure torque on that mantle of sufficient magnitude to explain LOD variations. These results indicate a linear dependence of the topographic torque on the CMB topography. However, it should

be noted that the torque acting on the CMB is proportional to the square of the flow speed. The flow speed considered for Earth is associated with the geodynamo and core convection, processes that are absent in Mars. Similarly, Rekier et al. (2025) investigated the form-drag effect, which may provide a viable explanation for the observed CMB coupling mechanisms.

Appendix A: Visual comparison of Earth and Mars nutations

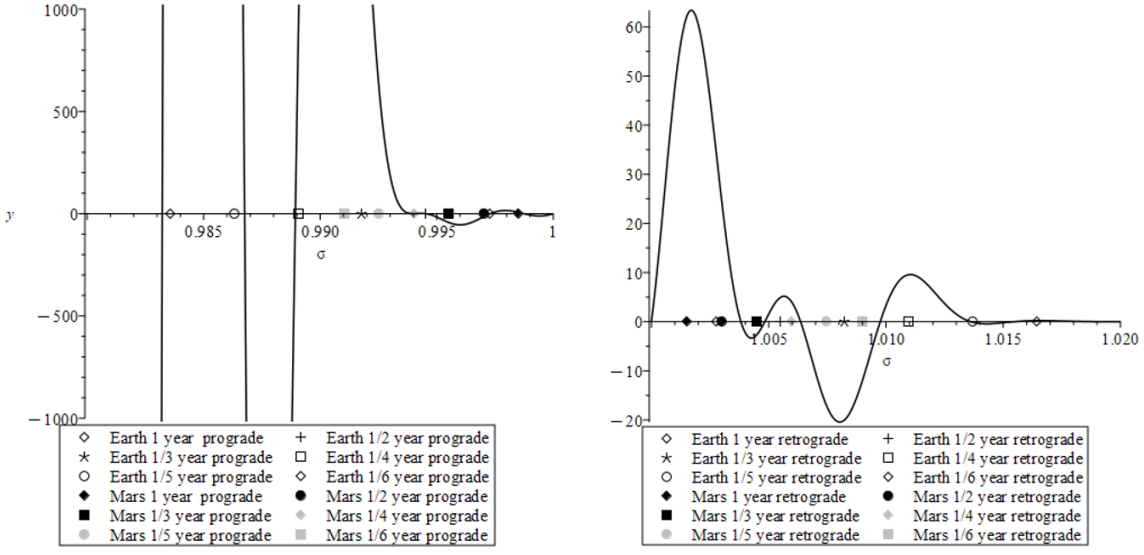

Figure A1. Determinant of the matrix $\mathbf{A_{nut}}$ involved in the system of Eqs. (14), showing the resonances where the curve is crossing zero. The nutation periods are expressed in a frame tied to the planet (in the diurnal frequency band). The prograde nutations are shown on the left graphics and the retrograde nutations are shown on the right. The nutation periods are shown with the symbols in the legend.

Code availability. The computations of the resonances with inertial waves presented in this work were carried out using the commercial software Maple. The Maple scripts employed are similar to those described in Puica et al. (2023) and Dehant et al. (2025), and are provided as supplementary material in those publications. The Green's functions used in this study are taken from Defraigne et al. (2001). Data: The data generated in this study are included in the tables presented in the main text and are therefore directly accessible within the article. No additional datasets were produced. The Mars geoid data used in this work were obtained from Zuber et al. (2000) and are publicly available via the publication.

Data availability. The data generated in this study are included in the tables presented in the main text and are therefore directly accessible within the article. No additional datasets were produced. The Mars geoid data used in this work were obtained from Zuber et al. (2000) and are publicly available via the repositories cited in that publication.

Author contributions. MFL and VD developed the analytical approach and computed the resonances and topographic torque. MP developed the initial Maple code used for the resonance computations. TVH provided expertise in the geophysical interpretation of the results.

Competing interests. The contact author has declared that none of the authors has any competing interests.

Disclaimer. Publisher's note: Copernicus Publications remains neutral with regard to jurisdictional claims made in the text, published maps, institutional affiliations, or any other geographical representation in this paper. The authors bear the ultimate responsibility for providing appropriate place names. Views expressed in the text are those of the authors and do not necessarily reflect the views of the publisher.

Acknowledgements. The authors thank Bernhard Steinberger and an anonymous reviewer for their careful and constructive reviews. The editor, Stephanie Werner, is also gratefully acknowledged for her handling of the manuscript and helpful comments.

Financial support. This research has been supported by the European Research Council, H2020 European Research Council (grant no. 855677) and the Fonds De La Recherche Scientifique – FNRS (grant no. PDR T.0066.20).

Review statement. This paper was edited by Stephanie C. Werner and reviewed by Bernhard Steinberger and one anonymous referee.

References

Baland, R. M., Yseboodt, M., Le Maistre, S., Rivoldini, A., Van Hoolst, T., and Dehant, V.: The precession and nutations of a rigid Mars, Celest. Mech. Dyn. Astr., 132, 47, https://doi.org/10.1007/s10569-020-09986-0, 2020.

Banerdt, W. B., Smrekar, S., Banfield, D., Giardini, D., Golombek, M., Johnson, C., Lognonné, P., Spiga, A., Spohn, T., Perrin, C., Stähler, S., Antonangeli, D., Asmar, S., Beghein, C., Bowles, N., Bozdag, E., Chi, P., Christensen, U., Clinton, J, Collins, G., Daubar, I., Dehant, V., Drilleau, M., Fillingim, M., Folkner, W., Garcia, R., Garvin, J, Grant, J, Grott, M., Grygorczuk, J, Hudson, T., Irving, J, Kargl, G., Kawamura, T., Kedar, S., King, S., Knapmeyer-Endrun, B., Knapmeyer, M., Lemmon, M., Lorenz, R., Maki, J, Margerin, L., McLennan, S., Michaut, C., Mimoun, D., Mittelholz, A., Mocquet, A., Morgan, P., Mueller, N., Murdoch, N., Nagihara, S., Newman, C., Nimmo, F., Panning, M., Pike, W., Plesa, A. C., Rodriguez, S., Rodriguez-Manfredi, J, Russell, C., Schmerr, N., Siegler, M., Stanley, S., Stutzmann, E., Teanby, N., Tromp, J, van Driel, M., Warner, N., Weber, R., and Wieczorek, M.: Initial results from the InSight mission on Mars, Nat. Geosci., 13, 183–189, https://doi.org/10.1038/s41561-020-0544-y, 2020.

Broquet, A., Plesa, A.-C., Klemann, V., Root, B. C., Genova, A., Wieczorek, M. A., Knapmeyer, M., Andrews-Hanna, J. C., and Breuer, D.: Glacial isostatic adjustment reveals Mars's interior viscosity structure, Nature, 639, 109–113, https://doi.org/10.1038/s41586-024-08565-9, 2025.

Buffett, B. A., Mathews, P. M., and Herring, T. A.: Modeling of nutation and precession: Effects of electromagnetic coupling, J. Geophys. Res., 107, https://doi.org/10.1029/2000JB000056, 2002.

Charalambous, C., Pike, W. T., Kim, D., Samuel, H., Fernando, B., Bill, C., and Lognonné, P.: Seismic evidence for a highly heterogeneous Martian mantle, Science, 389, 899–903, https://doi.org/10.1126/science.adk4292, 2025.

Cheng, Y., Dehant, V., Rivoldini, A., Rekier, J., and Bizouard, C.: Basic Earth Parameters from VLBI observations using Bayesian inversions in the time domain: updated insights of the Earth's interior, EGUsphere [preprint], https://doi.org/10.5194/egusphere-2025-4428, 2025.

Defraigne, P., Dehant, V., and Van Hoolst, T.: Steady-state convection in Mars' mantle, Planet. Space Sci., 49, 501–509, https://doi.org/10.1016/S0032-0633(00)00142-2, 2001.

Dehant, V., Van Hoolst, T., and Defraigne, P.: Comparison between the nutations of the planet Mars and the nutations of the Earth, Surv. Geophys., 21, 89–110, https://doi.org/10.1023/A:1006716529241, 2000.

Dehant, V., Folkner, W., Renotte, E., Orban, D., Asmar, S., Balmino, G., Barriot, J. P., Benoist, J., Biancale, R., Biele, J, Budnik, F., Burger, S., de Viron, O., Häusler, B., Karatekin, Ö., Le Maistre, S., Lognonné, P., Menvielle, M., Mitrovic, M., Pätzold, M., Rivoldini, A., Rosenblatt, P., Schubert, G., Spohn, T., Tortora, P., Van Hoolst, T., Witasse, O., and Yseboodt, M.: Lander Radioscience for obtaining the rotation and orientation of Mars, Planet. Space Sci., 57, 1050–1067, https://doi.org/10.1016/j.pss.2008.08.009, 2009.

Dehant, V., Le Maistre, S., Rivoldini, A., Yseboodt, M., Rosenblatt, P., Van Hoolst, T., Mitrovic, M., Karatekin, Ö., Marty, J. C., and Chicarro, A.: Revealing Mars' deep interior: Future geodesy missions using radio links between landers, orbiters, and the Earth, Planet. Space Sci., 59, 1069–1081, https://doi.org/10.1016/j.pss.2010.03.014, 2011.

Dehant, V., Banerdt, B., Lognonné, P., Grott, M., Asmar, S., Biele, J, Breuer, D., Forget, F., Jaumann, R., Johnson, C., Knapmeyer, M., Lefeuvre, M., Mimoun, D., Mocquet, A., Read, P., Rivoldini, A., Romberg, O., Schubert, G., Smrekar, S., Spohn, T., Tortora, P., Ulamec, S., and Vennerstrøm, S.: Future Mars geophysical observatories for understanding its internal structure, rotation, and evolution, Planet. Space Sci., 68, 123–145, https://doi.org/10.1016/j.pss.2011.10.016, 2012.

Dehant, V., Puica, M., Folgueira, M., Rekier, J, Trinh, A., and Van Hoolst, T.: Analytical computation of the total topographic torque at the Core-Mantle Boundary and its impact on nutations, Geophys. J. Int., 241, 474–494, https://doi.org/10.1093/gji/ggaf050, 2025.

Drilleau, M., Samuel, H., Rivoldini, A., Panning, M., and Lognonné, P.: Bayesian inversion of the Martian structure using geodynamic constraints, Geophys. J. Int., 226, 1615–1644, https://doi.org/10.1093/gji/ggab105, 2021.

Drilleau, M., Samuel, H., Garcia, R. F., Rivoldini, A., Perrin, C., Wieczorek, M., Lognonné, P., and Banerdt, W. B.: Constraints on lateral variations of Martian crustal thickness from seismological and gravity field measurements, Geophys. Res. Lett., 51, e2023GL105701, https://doi.org/10.1029/2023GL105701, 2024.

Goossens, S. and Sabaka, T. J.: Probing Lateral Density Variations in the Crust from Gravity and Topography: Applications to the Moon and Mars, The Planetary Science Journal, 6, 71, https://doi.org/10.3847/PSJ/adbaf0, 2025.

Greenspan, H. P.: The Theory of Rotating Fluids, Cambridge University Press, ISBN 10: 0521051479, ISBN 13: 9780521051477, 1969.

Guervilly, C. and Dormy, E.: The cross-over from viscous to inertial lengthscales in rapidly-rotating convection, Geophys. Res. Lett., 52, e2024GL111593, https://doi.org/10.1029/2024GL111593, 2025.

Khan, A., Ceylan, S., Van Driel, M., Giardini, D., Lognonné, P., Samuel, H., Schmerr, N. C., Stähler, S. C., Duran, A. C., Huang, Q., Kim, D., Broquet, A., Charalambous, C., Clinton, J. F., Davis, P. M., Drilleau, M., Karakostas, F., Lekic, V., McLennan, S. M.,

Maguire, R. R., Michaut, C., Panning, M. P., Pike, W. T., Pinot, B., Plasman, M., Scholz, J. R., Widmer-Schnidrig, R., Spohn, T., Smrekar, S. E., and Banerdt, W. B.: Upper mantle structure of Mars from InSight seismic data, Science, 373, 434–438, https://doi.org/10.1126/science.abf2966, 2021.

Khan, A., Huang, D., Durán, C., Sossi, P. A., Giardini, D., and Murakami, M.: Evidence for a liquid silicate layer atop the Martian core, Nature, 622, 718–723, https://doi.org/10.1038/s41586-023-06586-4, 2023.

Kiefer, W. S., Bills, B. G., and Nerem, R. S.: An inversion of gravity and topography for mantle and crustal structure on Mars, J. Geophys. Res.-Planet, 101, 9239–9252, https://doi.org/10.1029/95JE03699, 1996.

Konopliv, A. S., Park, R. S., and Folkner, W. M.: An improved JPL Mars gravity field and orientation from Mars orbiter and lander tracking data, Icarus, 274, 253–260, https://doi.org/10.1016/j.icarus.2016.02.052, 2016.

Koot, L., Dumberry, M., Rivoldini, A., De Viron, O., and Dehant, V.: Constraints on the coupling at the core–mantle and inner core boundaries inferred from nutation observations, Geophys. J. Int., 182, 1279–1294, https://doi.org/10.1111/j.1365-246X.2010.04711.x, 2010.

Le Maistre, S., Caldiero, A., Rivoldini, A., Yseboodt, M., Baland, R. M., Beuthe, M., Van Hoolst, T., Dehant, V., Folkner, W. M., Buccino, D., Kahan, D., Marty, J. C., Antonangeli, D., Badro, J, Drilleau, M., Konopliv, A., Péters, M. J., Plesa, A. C., Samuel, H., Tosi, N., Wieczorek, M., Lognonné, P., Panning, M., Smrekar, S., and Banerdt, W. B.: Spin state and deep interior structure of Mars from InSight radio tracking, Nature, 619, 733–737, https://doi.org/10.1038/s41586-023-06150-0, 2023.

MacRobert, T. M.: Spherical Harmonics: An Elementary Treatise on Harmonic Functions with Applications, Pergamon Press, ISBN 10: 0080121152, ISBN 13: 9780080121154, 1967.

Mathews, P. M., Herring, T. A., and Buffett, B. A.: Modeling of nutation and precession: new nutation series for nonrigid Earth and insights into the Earth's interior, J. Geophys. Res., 107, https://doi.org/10.1029/2001JB000390, 2002.

Monville, R., Cébron, D., and Jault, D.: Topographic drag at the core-mantle interface, J. Geophys. Res.-Sol. Ea., 130, e2024JB029770, https://doi.org/10.1029/2024JB029770, 2025.

Oliver, T. G., Blackman, E. G., Tarduno, J. A., and Calkins, M. A.: Turbulence in Earth's core generates large topographic torques on the mantle, Commun. Earth Environ., 6, 484, https://doi.org/10.1038/s43247-025-02451-6, 2025.

Puica, M., Dehant, V., Folgueira, M., Van Hoolst, T., and Rekier, J.: Analytical computation of the total topographic torque at the Core-Mantle Boundary and its impact on tidally driven Length-of-Day variations, Geophys. J. Int., 234, 585–596, https://doi.org/10.1093/gji/ggad077, 2023.

Reasenberg, R. D. and King, R. W.: The rotation of Mars, J. Geophys. Res., 84, 6231–6240, https://doi.org/10.1029/JB084iB11p06231, 1979.

Rekier, J., Triana, S. A., Barik, A., Abdulah, D., and Kang, W.: Constraints on Earth's Core-Mantle boundary from nutation, arXiv, https://doi.org/10.48550/arXiv.2507.01671, 2025.

Samuel, H., Drilleau, M., Rivoldini, A., Xu, Z., Huang, Q., Garcia, R. F., Lekić, V., Irving, J. C. E., Badro, J, Lognonné, P. H., Connolly, J. A. D., Kawamura, T., Gudkova, T., and Banerdt, W. B.: Geophysical evidence for an enriched molten silicate layer above Mars's core, Nature, 622, 712–717, https://doi.org/10.1038/s41586-023-06601-8, 2023.

Sasao, T., Okubo, S., and Saito, M.: A simple theory on the dynamic effects of a stratified fluid core upon nutational motion of the Earth, in: Nutation and the Earth's rotation, Proc. IAU Symposium, Kiev, Ukrainian SSR 1977, Dordrecht, D. Reidel Publishing Co., 165–183, https://doi.org/10.1007/978-94-010-9568-6_27, 1980.

Seuren, F., Triana, S. A., Rekier, J., Dehant, V., and Van Hoolst, T.: The influence of a stably stratified layer on the hydromagnetic waves propagating in the Earth's fluid outer core and their electromagnetic torques, Geophys. J. Int., 244, ggaf431, https://doi.org/10.1093/gji/ggaf431, 2026.

Shih, S. A., Triana, S. A., Rekier, J., and Dehant, V.: Turbulent Dissipation in the Boundary Layer of Precession-Driven Flow ina sphere, AIP Advances, 13, 075025, https://doi.org/10.1063/5.0146932, 2023.

Smith, D. E., Lerch, F. J., Nerem, R. S., Zuber, M. T., Patel, G. B., Fricke, S. K., and Lemoine, F. G.: An improved gravity model for Mars: Goddard Mars Model 1, J. Geophys. Res., 98, 20871–20890, https://doi.org/10.1029/93JE01839, 1993.

Smith, D. E., Sjogren, W. L., Tyler, G. L., Balmino, G., Lemoine, F. G., and Konopliv, A. S.: The Gravity Field of Mars: Results from Mars Global Surveyor, Science, 286, 94–97, https://doi.org/10.1126/science.286.5437.94, 1999.

Sohl, F., and Spohn, T.: The interior structure of Mars: Implications from SNC meteorites, J. Geophys. Res., 102, 1613–1635, https://doi.org/10.1029/96JE03419, 1997.

Stähler, S. C., Khan, A., Banerdt, W. B., Lognonné, P., Giardini, D., Ceylan, S., Drilleau, M., Duran, A. C., Garcia, R. F., Huang, Q., Kim, D., Lekic, V., Samuel, H., Schmerr, N. C., Sollberger, D., Stutzmann, E., Xu, Z., Antonangeli, D., Charalambous, C., Davis, P. M., Irving, J. C. E., Kawamura, T., Knapmeyer, M., Maguire, R. R., Marusiak, A. G., Panning, M. P., Perrin, C., Plesa, A.-C., Rivoldini, A., Schmelzbach, C., Zenhäusern, G., Beucler, E., Clinton, J. F., Dahmen, N., van Driel, M., Gudkova, T., Horleston, A., Pike, W. T., Plasman, M., and Smrekar, S. E.: Seismic detection of the martian core, Science, 373, 443–448, https://doi.org/10.1126/science.abi7730, 2021.

Wieczorek, M. A.: Gravity and Topography of the Terrestrial Planets, 2nd edn., in: Treatise on Geophysics, vol. 10, 153–193, https://doi.org/10.1016/B978-0-444-53802-4.00169-X, 2015.

Wieczorek, M. A., Beuthe, M., Rivoldini, A., and Van Hoolst, T.: Hydrostatic interfaces in bodies with nonhydrostatic lithospheres, J. Geophys. Res.-Planet, 124, 1410–1432, https://doi.org/10.1029/2018JE005909, 2019.

Wu, X. and Wahr, J. M.: Effects of non-hydrostatic core-mantle boundary topography and core dynamics on Earth rotation, Geophys. J. Int., 128, 18–42, https://doi.org/10.1111/j.1365-246X.1997.tb04069.x, 1997.

Zuber, M. T. and Smith, D. E.: Mars without Tharsis, J. Geophys. Res., 102, 28673–28685, https://doi.org/10.1029/97JE02527, 1997.

Zuber, M. T., Solomon, S. C., Phillips, R. J., Smith, D. E., Tyler, G. L., Aharonson, O., Balmino, G., Banerdt, W. B., Head, J. W., Johnson, C. L., Lemoine, F. G., McGovern, P. J., Neumann, G. A., Rowlands, D. D., and Zhong, S.: Internal Structure and Early Thermal Evolution of Mars from Mars Global

Surveyor Topography and Gravity, Science, 287, 1788–1793, https://doi.org/10.1126/science.287.5459.1788, 2000.